# GFP-Tagged Regulatory Light Chain Monitors Single Myosin Lever-Arm Orientation in a Muscle Fiber

Thomas P. Burghardt,*† Katalin Ajtai,* Daniel K. Chan,* Miriam F. Halstead,* Jinhui Li,* and Ye Zheng*
*Biochemistry and Molecular Biology, and †Physiology and Biomedical Engineering, Mayo Clinic College of Medicine, Rochester, Minnesota

ABSTRACT Myosin is the molecular motor in muscle-binding actin and executing a power stroke by rotating its lever arm through an angle of ~70° to translate actin against resistive force. A green fluorescent protein (GFP)-tagged human cardiac myosin regulatory light chain (HCRLC) was constructed to study in situ lever arm orientation one molecule at a time by polarized fluorescence emitted from the GFP probe. The recombinant protein physically and functionally replaced the native RLC on myosin lever arms in the thick filaments of permeabilized skeletal muscle fibers. Detecting single molecules in fibers where myosin concentration reaches 300 $\mu$M is accomplished using total internal reflection fluorescence microscopy. With total internal reflection fluorescence, evanescent field excitation, supercritical angle fluorescence detection, and CCD detector pixel size limits detection volume to just a few attoliters. Data analysis manages both the perturbing effect of the TIR interface on probe emission and the effect of high numerical aperture collection of light. The natural myosin concentration gradient in a muscle fiber allows observation of fluorescence polarization from C-term GFP-tagged HCRLC exchanged myosin from regions in the thick filament containing low and high myosin concentrations. In rigor, cross-bridges at low concentration at the end of the thick filament maintain GFP dipole moments at two distinct polar angles relative to the fiber symmetry axis. The lower angle, where the dipole is nearly parallel to fiber axis, is more highly populated than the alternative, larger angle. Cross-bridges at higher concentration in the center of the thick filament are oriented in a homogeneous band at ~45° to the fiber axis. The data suggests molecular crowding impacts myosin conformation, implying mutual interactions between cross-bridges alter how the muscle generates force. The GFP-tagged RLC is a novel probe to assess single-lever-arm orientation characteristics in situ.

## INTRODUCTION

Myosin heavy chain (MHC) is an elongated asymmetric molecule ~140 nm in length and consisting of three distinct regions: an N-terminal motor domain, a light chain binding neck region, and a C-terminal tail responsible for cargo binding and/or dimerization. The globular N-terminus contains the active site for MgATPase and an actin binding site with which it forms a cross-bridge with actin filaments. Myosin light chains (MLCs) arranged in tandem in the head-tail junction form a stabilizing collar around the heavy chain $\alpha$-helical neck thought to function as the lever arm (1–3). Myosin is an actin-dependent molecular motor that drives sarcomeric shorting and muscle contraction by transducing MgATP free energy into directed protein movement (4,5). MgATP hydrolysis is coupled to a series of conformational changes in myosin, which result in a cycle of attachment to the actin filament, strain development, protein translation, actin release, and reattachment (5). Myosin conformation change associated with strain development and protein translation, referred to as the power stroke, is shown in crystal structures by a lever arm rotation through ~70° (2,6). MLC association with the lever arm implies they follow the lever arm movement during the power stroke.

In muscle, the MHC C-terminus is a tail extending from the lever arm that regulates and participates in myosin self-assembly first into dimers and then a multimeric thick filament. The thick filament backbone is associated myosin dimer tail domains with heads projecting outward to permit interaction of the actin binding site with adjacent actin (thin) filaments. In skeletal muscle, thick and thin filaments organize into interacting arrays in the sarcomere where filaments overlap in the muscle sarcomere (7). The A-band in the sarcomere contains aligned thick filaments where myosin concentration reaches ~300 $\mu$M (8). Conditions imply skeletal myosin operates in a crowded environment.

Atomic structures of the MHC N-terminus containing one or both MLCs, called myosin subfragment 1 (S1), demonstrated the MLC's ideal location for detecting myosin conformation change during the power stroke (2,6). Much earlier it was demonstrated that MLCs were exchangeable (9,10). Combining these observations, an extrinsic-orientation-sensitive spectroscopic probe was introduced to the lever arm by modification of an isolated MLC that was introduced to the muscle by light chain exchange (11). Genetically engineered MLCs containing one cysteine residue were selectively modified at the SH group by a direction-reporting fluorescent probe and used to detect myosin dynamics in muscle fibers with time-resolved fluorescence polarization (12,13). More recently, fluorescent-labeled myosin regulatory light chain (RLC) and essential light chain (ELC) were simultaneously exchanged into fibers (14).

Green fluorescent protein (GFP) functions as a protein tag because its high stability permits it to fold and function as a fluorophore even when fused to other proteins through N- or C-terminal linkages. It is adaptable to in vivo studies because

*Submitted February 23, 2007, and accepted for publication May 14, 2007.*
Address reprint requests to T. P. Burghardt, E-mail: burghardt@mayo.edu.
Editor: Shin'ichi Ishiwata.

0006-3495/07/09/2226/14 $2.00
doi: 10.1529/biophysj.107.107433

it can be expressed in a wide variety of cells (15). The wild-type protein (wtGFP) has 238 residues (26 kDa molecular weight) and crystal structure consisting of an 11-stranded $\beta$-barrel surrounding a helix containing the fluorophore (15,16). The fluorophore is photobleaching-resistant and has a high quantum yield ($\sim$0.8) because it is positioned near the geometric center of the $\beta$-barrel where it is protected from solution-borne quenchers (17). Wild-type GFP (wtGFP) has two long wavelength absorption bands at $\sim$400 and 480 nm with emission at $\sim$510 nm (18). Polarized absorption from crystallized wtGFP molecules indicated the absorption dipole moment directions for the two visible bands relative to the atoms in the fluorophore and the crystallographic axes (19). Absorption and emission dipole moments were shown to be practically parallel in the longer wavelength band in wtGFP and wtGFP-tagged proteins (20,21).

Optical microscopic characterization of proteins in a biological assembly usually accumulates ensemble-averaged signals. For instance, polarized fluorescence emitted by fluorophores rigidly attached to myosin cross-bridges in a muscle fiber usually originates from the many probes within a detection volume that is large on a molecular scale. Active cross-bridges behave stochastically hence an ensemble of them in contraction will resemble a disordered system. Similarly, individual myosin cross-bridges in a fiber can rotate about the fiber symmetry axis without detectably affecting their ensemble-average orientation (22). Quick length changes in a contracting fiber (23–26), or, caged compounds releasing ATP or $Ca^{2+}$ to instantaneously trigger relaxation or contraction (27,28), act to synchronize cross-bridge movement and mitigate the stochastic averaging effect. Analysis of signal fluctuations via fluorescence correlation spectroscopy eliminates the ambiguities introduced by ensemble averaging because the signal is attributable to individual particles (29–31). Alternatively, emerging techniques detect protein movement from single fluorophores (32,33). They provide more insight into dynamics than the equivalent ensemble-based signal (34,35). Characterizing fluorescence from single motor proteins operating on substrate in vitro is the preferred means for characterizing motor function yet it does not necessarily represent the native system in a cell where molecular crowding is the norm (36,37).

In vitro versus in situ single molecule studies require different methods to isolate the molecule. In vitro, protein concentration is adjusted to isolate single molecules within the detection volume. In situ, protein concentration is fixed and single molecule detection requires use of novel fluorescence excitation and detection schemes that isolate one or just a few molecules in a high concentration milieu. We have used an approach based on total internal reflection fluorescence (TIRF) microscopy (38) that isolated $\sim$4 myosin cross-bridges in a muscle fiber (39). In TIRF microscopy, excitation laser light is incident on the glass side of a glass/water interface at angles greater than critical angle for total internal reflection. Although light is totally reflected, an evanescent field created in the water medium and decaying exponentially with distance from the interface, excites fluorophores within $\sim$100 nm of the surface (38). Focused (39,40) or unfocused (38,41) versions of prismless TIRF microscopy can provide detection volumes of $\sim$3 or $\sim$7 attoL ($10^{-18}$ L), respectively.

Human cardiac ventricular RLC (HCRLC) was GFP-tagged and exchanged into a permeabilized skeletal muscle fiber and did not noticeably impair fiber isometric force development when exchange efficiency was 60–70%. GFP fluorescence, detected from fibers where exchange efficiency was purposefully reduced to $<$10%, was confined to the A-band, indicating its association with the myosin lever arm. In rigor, myosin cross-bridges in the thick filament form a strong bond with thin filament actin giving the fiber its characteristic rigor stiffness. Using TIRF, we measured fluorescence polarization from a fiber in rigor by imaging an entire field of view containing many sarcomeres. Pixels in the image contained 1–6, or $\geq$7 GFPs that were distinguished by a characteristic change in fluorescence intensity per pixel versus accumulated photon count height. Low GFP density in the fiber ruled out the presence of GFP-GFP interactions, suggesting variable GFPs per pixel reflects spatially variable myosin concentration. GFP fluorescence intensity with $\geq$2 GFPs/pixel spatial probe distributions occupy the center of the A-bands where myosin concentration is constant and high while 1 GFP/pixel distributions occupy the edge of the A-bands where myosin concentration decreases rapidly to zero. Single GFP fluorescence polarization probability density (PD) indicated a highly ordered system and differed significantly from probe fluorescence polarization PD formed when $\geq$2 GFPs contributed.

Probe polarization PD reflects probe orientation PD weighted by the product of the amplitude-squared of the probe absorption dipole moment projected onto the excitation electric field polarization and the probe emission dipole moment projected onto the emission polarization analyzer orientation. The latter is further modified by perturbation of the emitted field due to the proximity of the TIR interface (42) and the ability of the microscopy objective to collect light from a solid angle about the probe (43). All optical factors accounted for, we modeled the probe polarization PD as a collection of normally distributed dipole moments. Free parameters in the modeling are the mean angle and distribution width. We find the myosin lever-arm orientation in rigor muscle depends on its position within the thick filament such that cross-bridges near the ends maintain the more inhomogeneous orientation distribution. It follows that either molecular crowding or local structural change at the thick filament ends disturbs the predominant homogeneous myosin lever arm orientation.

## MATERIALS AND METHODS

### Chemicals

Adenosine trisphosphate (ATP), Na-Azide, dithiothreitol (DTT), phenylmethylsulfonyl fluoride (PMSF), and porcine troponin are from Sigma (St.

Louis, MO). Bradford protein concentration assay is from Bio-Rad (Hercules, CA). SYPRO-Ruby fluorescent stain is from Invitrogen (Carlsbad, CA). Rabbit troponin C is from Life Diagnostics (West Chester, PA). Leupeptin, chymostatin, and pepstatin are from Roche Applied Sciences (Indianapolis, IN). All chemicals are reagent grade or Ultra-Pure if available.

## GFP-tagged HCRLC construction

The cDNA of wild-type HCRLC cloned into pET-3d (Novagen, Gibbstown, NJ) plasmid vectors were a generous gift from Dr. D. Szczesna-Cordary, University of Miami (44). The cDNA of the protein was transformed into BL21 (DE3) expression host cells. Ten milliliters of overnight culture at 37°C was used to inoculate 500 ml of LB medium with 10 $\mu$g/ml ampicillin. Isopropyl-1-thio-$\beta$-D-galactopyranoside was added to 1 mM when the $A_{600}$ reached to 0.8–1.0. Cultures continue to grow for 6 h. Cells were harvested by centrifugation at 6300 $\times$ *g* for 20 min. Fig. 1 *A* compares HCRLC expression level before and after transformation. No protein band with molecular weight similar to HCRLC was observed in DE3 cells before transformation. The cells were harvested and pellets lysed in 20 ml of lysis buffer (2 M urea, 25 mM Tris-HCl, 0.1 mM PMSF, 1 mM dithiothreitol, 0.001% $NaN_3$, pH 7.5) bringing the total volume to 30 ml that was sonicated on ice for 10 min. The solution was centrifuged at 12,000 $\times$ *g* at 4°C for 45 min. The supernatant was incubated with Q-Sepharose (Sigma) at room temperature for 30 min and centrifuged at 3100 $\times$ *g* for 10 min. The proteins were eluted with a 50-ml salt gradient of 0–300 mM KCl. The eluted protein was further purified by a DE-52 column (Whatman, Florham Park, NJ) with the process similar to that of Q-Sepharose (44). The protein eluted from the DE-52 column was dialyzed at 4°C overnight in 1 liter of 20 mM imidazole, 50 mM NaCl, and 0.1 mM PMSF, pH 7.5. The final purity of the proteins was tested using 15% SDS-PAGE stained with Coomassie blue. Fig. 1 *B* (Gel 1) shows the purified HCRLC.

The wild-type and mutant cDNA were amplified by PCR and cloned into vector pcDNA3.1/NT-GFP-TOPO or pcDNA3.1/CT-GFP-TOPO (Invitrogen) to make constructs with the GFP located on either the N- or C-terminus. The fragments were further subcloned into pET-3d (Novagen) plasmid vector for expressing the GFP-tagged proteins. Several HCRLC/GFP linkers were tried with the following sequences producing the folded GFP-tagged light chains,

$$\text{GFP}\{\text{KLGSGSGS}\}\text{HCRLC Construct plasmid 1,}$$
$$\text{HCRLC}\{\text{GGGGGGVPVEK}\}\text{GFP Construct plasmid 2.}$$

We transformed these plasmids into BL21 (DE3) as just described. Fig. 1 *B* (Gel 2) shows the purified, C-terminal GFP-tagged construct, HCRLC-GFP.

## Fiber preparation and light-chain exchange

Solutions used are listed in Table 1. Rabbit *psoas* muscle fibers were obtained as described earlier (45) and kept in bundles of 100–200 fibers in a glycerinating solution (Relax solution containing 50% glycerol, pH 7) at −20°C and stored for up to several weeks. Just before a measurement, fiber bundles were incubated in FPS (fiber preparation for skinning) solution for 1 h on ice with stirring then transferred to Skinning solution and incubated on ice with stirring for 1 h. The bundles were washed in FPS then Rigor solution before transferring to Dissecting solution (Rigor solution containing 50% glycerol, pH 7) for dissection into single fibers.

Clean glass #1 coverslips were sonicated for 10 min in ethanol then plasma-cleaned (Harrick Plasma, Ithaca, NY) for 15–30 min. A plasma-cleaned coverslip was placed on a 1′′ $\times$ 3′′ brass slide with a hole cut out permitting the objective from the inverted microscope to reach the coverslip. A water tight chamber was constructed on top of the plasma-cleaned coverslip as shown in Fig. 2. Two opposing sides of the chamber were formed by narrow silicon grease strips extruded from a pipette tip at approximately the thickness of a coverslip. The grease strips ran the length of the bottom coverslip. Single fibers were placed on the plasma-cleaned coverslip and bathed in Prerigor solution. Chamber top was formed by another #1 thickness coverslip made shorter than the bottom coverslip by slicing off two 2-mm-wide rectangles using a diamond-tipped pen. The rectangular slices were placed on the outer edges of the bottom coverslip to act as spacers between chamber top and bottom then the top slide was put into position. Two other opposing sides of the chamber were left open, allowing solution exchange. Spacers are shown taller for clarity in Fig. 2. In an actual experiment, the long fiber dimension runs parallel to the silicone strips to facilitate solution exchange. The chamber contains ~50 $\mu$L.

The RLC exchange protocol was derived with minor changes from a previously described method (46). The approach is to extract native RLC with Extracting solution containing EDTA chelating the divalent metal ions stabilizing RLC binding to myosin and to replace it with the exogenous protein. Troponins are also extracted by this treatment impairing fiber contractility and $Ca^{2+}$ regulation. The troponins are reconstituted into the fiber in the final step of the procedure. In the following, solution replacement implies ≥3 exchanges of the chamber volume with new solution. The preparation is held at 10°C except where noted otherwise.

Light chain exchange

1. Incubate in Prerigor for 3 min.
2. Replace with Rigor solution and incubate for 3 min.
3. Replace with Extract solution and incubate for 3 min.
4. Replace with Extract + GFP-tagged RLC (0.1–0.5 $\mu$g/$\mu$L) + 10 mM fresh DTT and increase temperature to 30°C for 30 min.
5. Decrease temperature to 10°C and replace with Rigor solution (5–10 volumes) for 3 min.

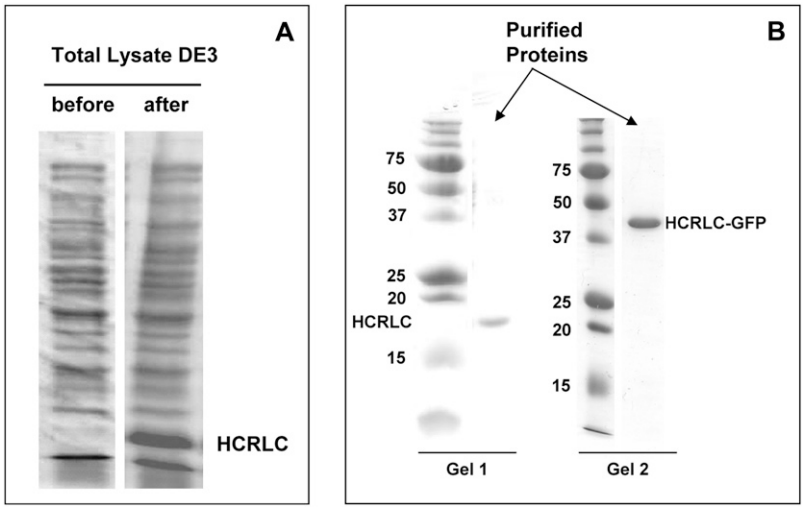


FIGURE 1 (*A*) SDS-PAGE of the total DE3 cell lysate proteins before and after transformation with cDNA for the wild-type HCRLC. (*B*) SDS-PAGE of standards, purified wild-type HCRLC (Gel 1), and purified HCRLC-GFP (Gel 2). The purified proteins are homogeneous light chains.

**TABLE 1 Light-chain exchange solutions**

| Solution | FPS | Skinning | Prerigor | Rigor | Extract | Relax | Preactive | Active |
|---|---|---|---|---|---|---|---|---|
| Imidazole | 6 | 6 | 25 | 10 | — | 25 | 25 | 25 |
| EGTA | 5 | 5 | 7.2 | 2.5 | — | 5 | 0.2 | — |
| ATP | 5 | 5 | 0.1 | — | — | 5 | 5 | 5 |
| CrP* | — | — | 5 | — | — | 5 | 5 | 5 |
| Mg acetate | 8 | 8 | 1.5 | 2.2 | — | 7 | 7 | 7 |
| KPr† | 70 | 70 | 91.6 | 130 | 50 | 80 | 90 | 80 |
| EDTA | — | — | — | — | 20 | — | — | — |
| NaAzide | 1 | 1 | — | — | — | — | — | — |
| KPi | — | — | — | — | 10 | — | — | — |
| PMSF | 0.2 | 0.2 | 0.1 | 0.1 | 0.1 | 0.1 | 0.1 | 0.1 |
| Leupeptin ($\mu$g/mL) | 8 | 8 | 8 | 8 | 8 | 8 | 8 | 8 |
| DTT | 1 | 1 | 1 | 1 | 1 | 1 | 1 | 1 |
| Triton X100 (%) | — | 0.5 | — | — | — | — | — | — |
| CrPk‡ (mg/mL) | — | — | — | — | — | — | 1 | — |
| $CaCl_2$ | — | — | — | — | — | — | — | 0.1 |
| *Ionic Str.* | | | *150* | *151* | *150* | *159* | *155* | *150* |

Concentrations in mM except where noted otherwise.
*Creatine phosphate.
†Potassium propionate.
‡Creatine phosphokinase.

Troponin replacement

6. Replace with Rigor solution+Troponin (0.5 mg/ml) and incubate for 10 min.
7. Replace with Rigor solution+Troponin C (0.5 mg/mL) and incubate for 5 min.

Measurement

8. Conduct tension measurements on 0.5 $\mu$g/$\mu$L HCRLC-GFP exchanged single fibers or optical measurements on 0.1–0.5 $\mu$g/$\mu$L HCRLC-GFP exchanged single fibers.

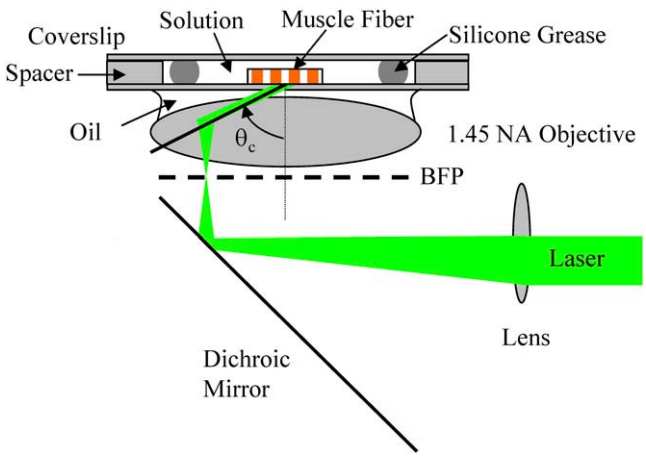


FIGURE 2 Total internal reflection fluorescence (TIRF) microscopy. The excitation laser light is focused on the back focal plane of a 1.45 numerical aperture (NA) objective and incident on the glass side of a glass/water interface at angles greater than critical angle, $\theta_c$, for TIR. The evanescent field, created in the water medium and decaying exponentially with distance from the interface, excites fluorophores within ~100 nm of the surface. The muscle fiber contacts the glass coverslip and is contained in a 50 $\mu$L chamber defined by the spacer width and the silicone grease restricting aqueous fluid to the fiber containing volume. Solution surrounding the fiber is exchanged by capillary action through openings at the edges of the top coverslip.

Light-chain exchange efficiency was measured by detecting loss of native RLC and replacement with GFP-tagged HCRLC by SDS-PAGE on proteins extracted from the muscle fibers as described previously (47). Fig. 3 shows the SYPRO Ruby stained (Bio-Rad, Hercules, CA) SDS-PAGE for HCRLC-GFP exchanged into the fiber. Lanes are: (Fig. 3 *A*) untreated fiber, (Fig. 3 *B*) after HCRLC-GFP exchange, (Fig. 3 *C*) Troponin C, (Fig. 3 *D*) HCRLC-GFP, (Fig. 3 *E*) Actin, and S molecular weight standards. Lanes *A* and *B* are from adjacent segments of the same fiber.

After exchange (*B*), the skeletal RLC band is clearly less intense than in the control fiber (*A*), the band corresponding to Troponin C (*C*) is lost, and a new band corresponding to HCRLC-GFP (*D*) appears. Actin is not extracted by the RLC exchange protocol and is used as the standard to normalize intensities in lanes *A* and *B*. SYPRO Ruby intensities are proportional to molecular weights (see Supplementary Material). The fraction of HCRLC in HCRLC-GFP is 0.42 based on the molecular weight and the incorporated HCRLC-GFP is 0.64 ± 0.07 of the total RLC in the native fiber. Thus 60–70% of myosin heads contained a HCRLC-GFP. The skeletal RLC fraction remaining after extraction was 0.37 ± 0.08, consistent with stoichiometric exchange by HCRLC-GFP.

Tension measurements were performed as described previously (25) on control and exchanged single muscle fibers to investigate how HCRLC or GFP-tagged HCRLC substitution affects contractility. Fig. 4 compares peak isometric force per cross-sectional area for the preextraction control (*PRE*), post-light chain exchange (*PO*), and after troponin reconstitution (*RE*). We find that light-chain exchange diminishes force to approximately half of control but reconstitution with troponin restores most of the contractility. Exchange/reconstitution restores 87 and 81% of control contractility for HCRLC and GFP-tagged HCRLC, respectively. This is comparable to effects observed with rhodamine-labeled RLC exchange (13). Error bars show standard error of the mean for $n = 4$–8.

## TIRF microscopy

The microscope setup is shown schematically in Fig. 2. Excitation laser light is focused on the back focal plane of a 1.45 numerical aperture (NA) objective and incident on the glass side of a glass/water interface at angles greater than critical angle, $\theta_c$, for TIR. Although light is totally reflected, an evanescent field created in the water medium and decaying exponentially with distance from the interface, excites fluorophores within ~100 nm of the

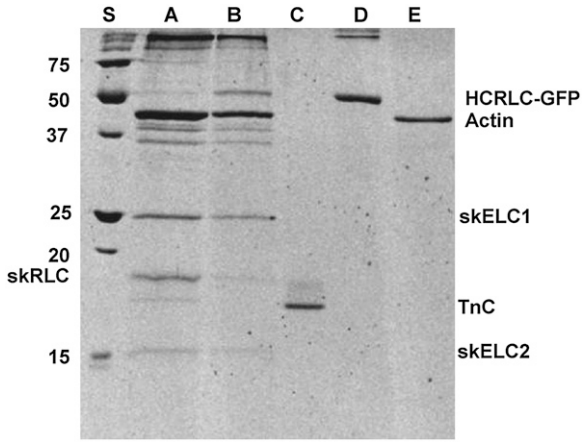


FIGURE 3 SDS-PAGE of fiber extract with proteins visualized using SYPRO-Ruby fluorescent stain. Lane: *S*, molecular weight standards; *A*, untreated fiber; *B*, after HCRLC-GFP exchange; *C*, Troponin C; *D*, HCRLC-GFP; and *E*, Actin.

surface (38). This version of TIRF provides detection volumes of ~7 attoL ($10^{-18}$ L) (39).

The TIR interface affects probe emission. Fig. 5 shows an emitting fluorophore, $\boldsymbol{\mu}$, in the aqueous medium near a dielectric interface (water/glass). The probe dipolar emission field is the superposition of propagating transverse waves forming the far-field and nonpropagating longitudinal (evanescent) waves forming the near-field. The near-field is not detected unless perturbed by the nearby interface creating detectable propagating transverse waves (42). Converted near-field propagating waves appear in the glass medium at angles beyond critical angle and are referred to as supercritical angle fluorescence (SAF) (40). Oil immersion objectives with NA≳1.3 capture SAF. Subcritical angle fluorescence is from far-field emission. Detectable SAF emission intensity decreases with the probe distance from the interface, thereby creating a second level of spatial selectivity favoring

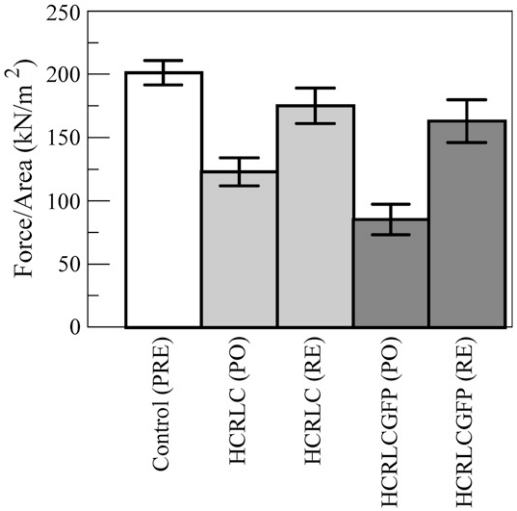


FIGURE 4 Peak isometric force per fiber cross-sectional area in units of kiloNewtons/meter$^2$ for the preextraction control (*PRE*), post-light chain exchange (*PO*), and after troponin reconstitution (*RE*) conditions. Exchanged light chains are the native HCRLC (*light gray*) or the GFP-tagged HCRLC (*dark gray*). Error bars show standard error of the mean for $n = 4$–8.

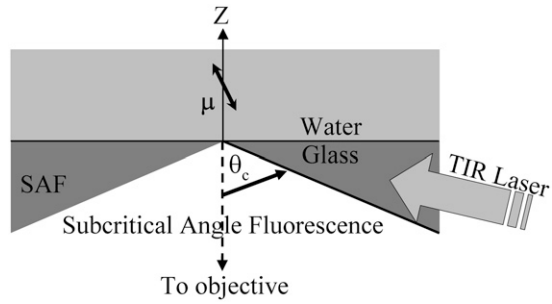


FIGURE 5 Dielectric interface supporting TIR also affects probe emission into the glass medium where the high NA microscope objective collects fluorescence. The emitting fluorophore ($\boldsymbol{\mu}$) in the aqueous medium is near a dielectric interface. The probe dipolar emission field is the superposition of propagating transverse waves forming the far-field and nonpropagating evanescent waves forming the near-field. The emitted far field is detected as subcritical angle fluorescence by any objective with finite aperture. The near-field is not detected unless perturbed by the interface to create detectable propagating transverse waves. Converted near-field propagating waves appear in the glass medium at angles beyond critical angle, $\theta_c$, and are referred to as supercritical angle fluorescence (SAF). Oil immersion objectives with NA≳1.3 capture SAF.

probes nearest to the interface in addition to the exponential decay from the exciting field. The TIR interface affects polarized emission, requiring correction factors for emission collection efficiency like those derived for a high aperture objective (43). The corrections are derived in Results.

Excited fluorescence collected by the objective is filtered, analyzed for polarization, and formed into an image by the microscope tube lens at a 12 bit CCD camera (Hamamatsu Orca ER Cooled Digital CCD Camera). Camera pixels (6.45 × 6.45 $\mu$m) were binned 2 × 2 to match objective resolution defined by its point spread function such that image deconvolution reiterates the original. Pixel size together with the evanescent field depth defines an object space detection volume of ~$8.2 \times 10^6$ nm$^3$ for the 60× objective (39). The detection volume contains ~1480 RLCs in the center of the A-band.

## Fluorescence polarization

Microscopic fluorescence polarization contains polarization selective absorption and emission effects both contributing to the sensitivity of the signal to orientation of the emitting dipole. Fluorescence polarization is expressed as ratios to eliminate dependence on absolute intensities such that

$$P_{\parallel} = \frac{F_{\parallel,\parallel} - F_{\parallel,\perp}}{F_{\parallel,\parallel} + F_{\parallel,\perp}} \qquad P_{\perp} = \frac{F_{\perp,\perp} - F_{\perp,\parallel}}{F_{\perp,\perp} + F_{\perp,\parallel}}, \tag{1}$$

where $F_{i,j}$ is fluorescence intensity for incident excitation electric field polarization $i$ and fluorescence emission electric field polarization $j$. For a muscle fiber, $\parallel$ (parallel) or $\perp$ (perpendicular) means relative to the fiber symmetry axis.

Polarized electric field intensities illuminating the fiber in contact with the TIR interface are shown in Fig. 6, where ($x$,$y$,$z$) are fiber-fixed coordinates with $z$- parallel to the fiber symmetry axis, $y$- normal to the interface, and $x$- in the plane of the interface. The perpendicular field has two components due to the elliptical polarization of the evanescent field but intensity is predominantly polarized normal to the interface (along the $y$ axis) (48). The $\perp$-polarization defines an exciting field that is predominantly perpendicular to both orientations of the emission analyzer. This is unlike epi-illumination fluorescence polarization where exciting light polarization is never perpendicular to both orientations of the emission polarization analyzer.

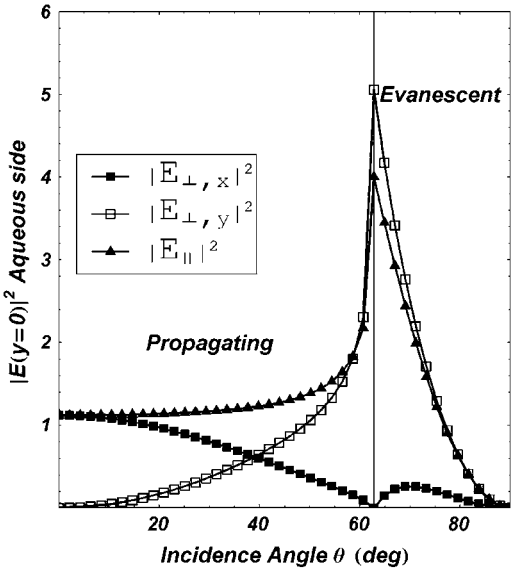


FIGURE 6 Excitation field profile at the interface but on the aqueous side as a function of incidence angle and field polarization. The excitation laser beam is incident on the glass/water interface from the glass side. The (*x*,*y*,*z*) coordinates are fiber fixed coordinates with *z*- parallel to the fiber symmetry axis, *y*- normal to the interface, and *x*- in the plane of the interface. Axes origin is on the interface. Light incident at subcritical angles produces a field propagating into the aqueous medium. Light incident at supercritical angles produces an evanescent field in the aqueous medium. The evanescent field propagates in the plane of the interface but not into the aqueous medium.

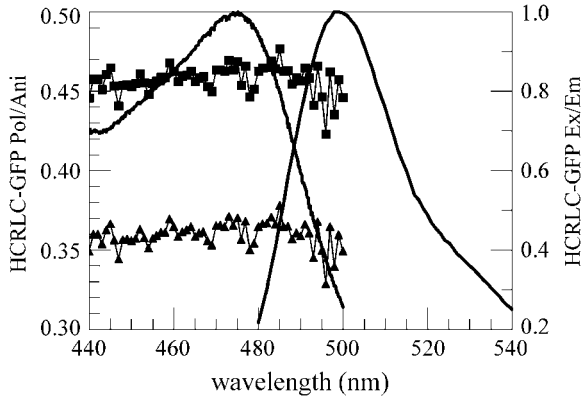


FIGURE 7 Excitation (*left line curve*) and emission (*right line curve*) spectra from HCRLC-GFP in solution. The polarization anisotropy, $r = (F_{\parallel} - F_{\perp})/(F_{\parallel} + 2F_{\perp})$ (*triangles*), and polarization, $P = (F_{\parallel} - F_{\perp})/(F_{\parallel} + F_{\perp})$ (*squares*), are also shown.

## RESULTS

### GFP spectroscopy

Fig. 7 shows excitation (*left*) and emission (*right*) spectra from HCRLC-GFP in solution. The polarization anisotropy, $r = (F_{\parallel} - F_{\perp})/(F_{\parallel} + 2F_{\perp})$ (*triangles*), is slightly lower than the theoretical maximum of 0.4, but larger than GFP or GFP-tagged actin in solution, $r = 0.32$ or 0.33 (21), and consistent with polarization relaxation due to rotation of the entire fused protein (49,50). It appears that GFP does not rotate independently from HCRLC in HCRLC-GFP. Also shown is the polarization $P = (F_{\parallel} - F_{\perp})/(F_{\parallel} + F_{\perp})$ (*squares*) that has a theoretical maximum of 0.5. Identical experiments were conducted on the N-terminal-tagged construct (GFP-HCRLC). GFP-HCRLC has identical polarization anisotropy, indicating no apparent GFP mobility independent of HCRLC. The GFP-HCRLC gives the more intense fluorescence.

### Single molecule fluorescence polarization from skeletal muscle fibers

HCRLC-GFP was exchanged into a skeletal fiber and observed under rigor conditions with TIRF. We collected emission at >500 nm from excitation at 488 nm. Evanescent excitation light propagates in the interface plane and normal to the fiber with electric field polarization parallel (*s*-polarized incident) or perpendicular (*p*-polarized incident) to the fiber axis. Images with analyzing polarizer parallel or perpendicular to the fiber axis were collected sequentially in 1 s exposures. Images were processed by subtracting background estimated by averaging the photon counts from empty regions surrounding the fiber. GFP photobleaching was not detectable for the excitation level used. In separate experiments using identical exciting light conditions the photobleaching rate for HCRLC-GFP exchanged into fibers was 0.001 $s^{-1}$, implying ~2 min of continuous illumination decreases emission intensity by ~10%.

Fig. 8 indicates normalized change in photon counts per pixel, $W = \Delta[(F_{\perp,\perp} + F_{\perp,\parallel})/\text{pixel}]$, ensemble-averaged $P_{\perp}$ ($\langle P_{\perp} \rangle$), and $P_{\perp}$ standard deviation versus accumulated photon count (PC) window height. The window admits pixels containing photon counts greater than background but less than or equal to the value plotted on the *x* axis. *W* levels off to zero or near-zero slope in ~100-count intervals, indicating domains of window heights where photons from 1–6, or ≥7 molecules are selectively acquired in single pixels. Intervals of level slope vary somewhat with window height because $F_{\perp,\perp} + F_{\perp,\parallel}$ is not strictly independent of probe orientation in the oriented HCRLC-GFP labeled muscle-fiber system and because the evanescent field is spatially inhomogeneous over the field of view due to scattering. $\langle P_{\perp} \rangle$ versus window height confirms that probe orientation varies with the detected probes per pixel, i.e., with probe or cross-bridge concentration. Simulation confirms *W* versus *PC* window height identifies the threshold for single molecule emission and qualitatively reproduces the curve shown in Fig. 8 for *W* versus accumulated *PC* window height (see Supplementary Material).

Polarization ratio $P_{\perp}$ is minimal for single molecules then increases asymptotically to $-0.28 \pm 0.14$ as molecules in the detected volume increase. Single molecule ensemble-average ± standard deviation $\langle P_{\perp} \rangle_1 = -0.54 \pm 0.21$. The equivalent measurement for $P_{\parallel}$ is $\langle P_{\parallel} \rangle_1 = 0.49 \pm 0.22$. For the TIRF instrument described, including the effect of K-factors on

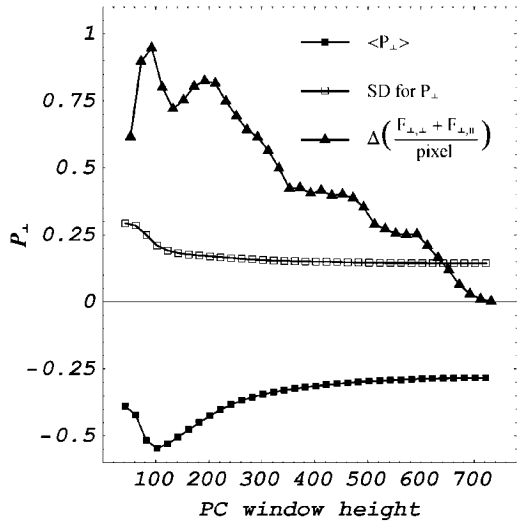


FIGURE 8 Change in photon counts per pixel, $W = \Delta[(F_{\perp,\perp} + F_{\perp,\parallel})/\text{pixel}]$, versus accumulated photon count window height indicates photon count thresholds where 1–6, and ≥7 GFPs are in the detection volume. The window admits pixels containing photon counts higher than background but less than or equal to the height plotted on the $x$ axis. Ensemble-averaged $P_\perp$ ($\langle P_\perp \rangle$), and $P_\perp$ standard deviation versus photon count window height indicates how these parameters change with GFP number in the detection volume.

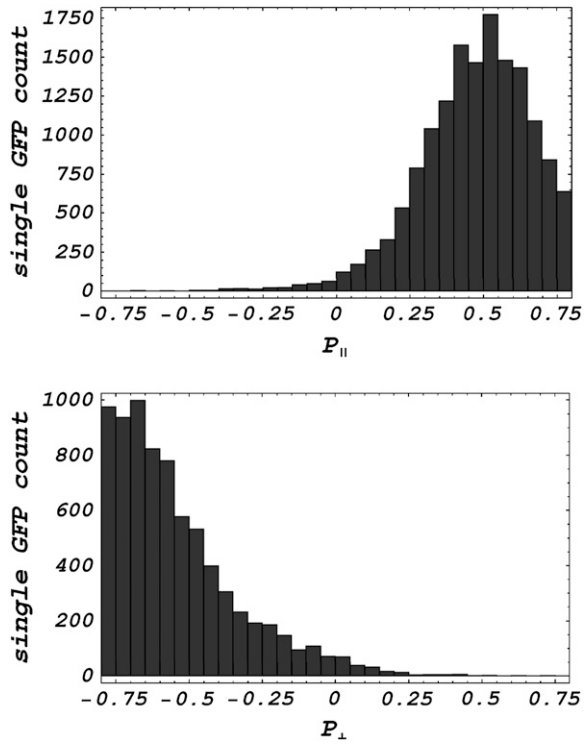


FIGURE 9 Single GFP molecule count versus $P_\parallel$ (*top*) and $P_\perp$ (*bottom*). The histograms represent the experimental $P_\parallel$ and $P_\perp$ probability densities.

measured polarized emission (see TIRF Emission Characteristics), both polarization ratios will fall within the range $-0.8 \le P \le 0.8$ and a statically disordered ensemble gives $\langle P_\parallel \rangle = 0.284$ and $\langle P_\perp \rangle = 0.004$.

Fig. 9 shows histograms for single GFP molecule count versus $P_\parallel$ (*top*) and $P_\perp$ (*bottom*), indicating PDs corresponding to ensemble-averages $\langle P_\parallel \rangle_1$ and $\langle P_\perp \rangle_1$. At higher myosin concentration where there are two GFPs per pixel, PDs gave $\langle P_\parallel \rangle_2 = 0.37 \pm 0.11$ and $\langle P_\perp \rangle_2 = -0.40 \pm 0.15$. We estimated dipole orientations simultaneously corresponding to the $P_\parallel$ and $P_\perp$ PDs using a Monte Carlo simulation for normally distributed probe dipole orientations,

$$p(\alpha, \alpha_0, \sigma_\alpha, \beta, \beta_0, \sigma_\beta) = \frac{\text{Exp}\left[\frac{-(\alpha-\alpha_0)^2}{2\sigma_\alpha^2}\right]}{\sqrt{2\pi}\sigma_\alpha} \frac{\text{Exp}\left[\frac{-(\beta-\beta_0)^2}{2\sigma_\beta^2}\right]}{\sqrt{2\pi}\sigma_\beta}, \quad (2)$$

with mean azimuthal and polar angles, $\alpha_0$ and $\beta_0$, measured relative to the fiber axis and distribution widths, $\sigma_\alpha$ and $\sigma_\beta$. Simulation generates 400 normally distributed random configurations for each choice of $\alpha_0$, $\sigma_\alpha$, $\beta_0$, and $\sigma_\beta$ falling on a four-dimensional grid with $0 \le \alpha_0$, $\sigma_\alpha \le \pi$ and $0 \le \beta_0$, $\sigma_\beta \le \pi/2$. Grid resolution is 10 or 5° for azimuthal or polar degrees of freedom, respectively.

Fluorescence polarization ratios are equal for any combination of $\alpha_0$, $\alpha_0 + \pi$, $\beta_0$, and $\pi - \beta_0$ because the fluorescence intensity originates from an electric transition in the GFP dipole. Thus, grid limits on $\alpha_0$ and $\beta_0$ do not affect generality of the results. Distribution-width limits were decided from experience fitting the data. There are $>10^5$ total probe orientation configurations generated from which ensemble-averaged probe polarization PDs were computed for comparison with the two observed ensemble-averaged PDs. Shown below are the best choice configurations corresponding to ≲0.2% of all configurations generated.

For all GFPs per-pixel myosin cross-bridge concentrations, $\alpha_0$ and $\sigma_\alpha$ are distributed nearly evenly over their domain (data not shown). Although each cross-bridge binds at a distinct azimuthal coordinate, the probe ensemble has rotational symmetry about the fiber axis, resulting in the observed distribution. In contrast, at single GFP per pixel myosin concentration, $\beta_0$ and $\sigma_\beta$, are distributed as shown by the histograms in Fig. 10, *A* and *B*. Distribution width is centered on 30–35° while the mean polar angle has discrete values at 5–10° and 25–30°. The 25–30° value is approximately half as frequent as the 5–10° orientation. The data shows that single cross-bridges at low concentration bind to actin filaments at two orientations.

Fig. 10, *C* and *D*, show $\beta_0$ and $\sigma_\beta$ PDs for the two GFPs per pixel myosin concentration. Probe distribution width is centered on 10–15° and only one mean polar angle centered on 40–45° is observed. Thus the bimodal distribution characteristic to probes at low myosin concentration becomes homogeneous at higher concentration. Higher cross-bridge concentration (≥3 GFPs per detection volume) behaves similarly to the two-GFP case.

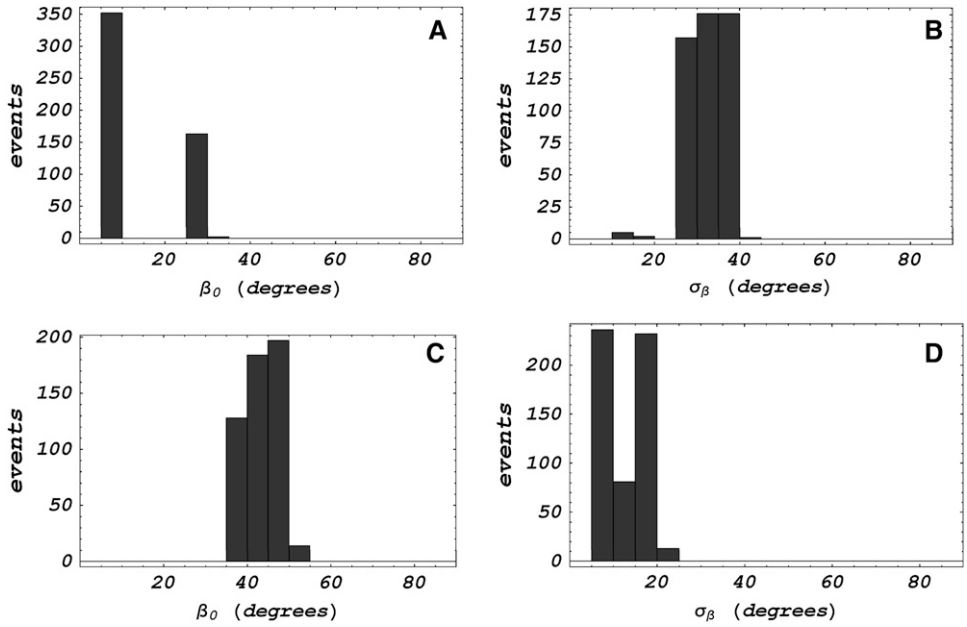


FIGURE 10 (*A*,*B*) Probability densities of single GFP dipoles on cross-bridges in rigor at low concentration for the average polar angle, $\beta_0$, and width, $\sigma_\beta$, defined by Eq. 2. (*C*,*D*) Equivalent to panels *A* and *B*, but for the two-GFPs/pixel cross-bridge concentration case. The bimodal probability density for $\beta_0$, characteristic to probes at low cross-bridge concentration, becomes homogeneous at higher cross-bridge concentration.

Fig. 11 (*top*) indicates the spatial distribution of single HCRLC-GFP in an exchanged fiber. Pixels containing single GFP are depicted in blue over the grayscale total fluorescence intensity from the fiber. Pixels containing single molecules are at the A-band periphery where myosin concentration drops to zero from its peak value of ~300 $\mu$M in the A-band center. Pixels containing two or more GFPs are distributed closer to the A-band center where myosin concentration is higher. Fig. 11 (*bottom*) shows the GFP fluorescence from the entire fiber sample. Fiber intensity has the speckled appearance of discrete labeling points expected from a sparsely-labeled sample (51).

We also experimented with GFP-HCRLC exchanged fibers. GFP-HCRLC exchanged into fibers under conditions identical to that used for HCRLC-GFP, emits with higher absolute fluorescence intensity. $P_\parallel$ from the GFP-HCRLC exchanged fiber is similar to that from free GFP-HCRLC (unlike its HCRLC-GFP counterpart), suggesting the GFP is disordered and possibly independently mobile in this case. Exchanged GFP-HCRLC is suitable for detection of myosin location and translation with an intensity signal not strongly influenced by cross-bridge orientation.

## Cross-bridge fluorescence polarization compared from fibers in rigor and relaxation

Fluorescence polarization images from heavily HCRLC-GFP exchanged fibers in rigor and relaxation were compared to assess the effect of strong cross-bridge binding to actin on GFP orientation. Strongly actin-bound rigor cross-bridges are detached from actin by incubation of the fiber in Relaxing solution containing ATP (Table 1). Fig. 12 shows 300 × 100 pixels rectangular areas of the images. The $P_\parallel$ and $P_\perp$ (Eq. 1) images show significant spatial inhomogeneity in rigor compared to that in relaxation demonstrating that strong cross-bridge binding to actin affects GFP orientation. The histogram for all pixels inside the area (30,000) are shown in Fig. 13 as pixel count versus $P_\parallel$ or $P_\perp$. Relaxed polarization ratios are narrowly distributed and centered on the value characteristic to a statically disordered probe. Rigor polarization ratios are broadened and shifted from the random distribution, toward a higher $P_\parallel$ or lower $P_\perp$-value. The histograms are not sorted on GFP per pixel number and the labeling stoichiometry, estimated to be 60–70% of RLC sites, is much higher than that for the fiber shown in Fig. 11. Intensity images (data not shown) corresponding to these polarization images do not show the speckled appearance of discrete labeling points seen in Fig. 11.

The higher fluorescence intensity signals in the heavily GFP labeled fibers allow direct observation of spatially variable rigor cross-bridge orientation due to interaction with actin. The distinctive white line in the H zone of the $P_\perp$ image shows higher polarization (closer to the statically disordered $P_\perp$) where myosin heads do not overlap with the thin filament. The lighter regions at the A-band/I-band interface of the $P_\parallel$ image shows higher polarization (more distant from the statically disordered polarization) where myosin heads are in lower concentration. The latter observation reinforces our conclusion from the single GFP measurements that cross-bridges at low concentration bind to actin with larger $P_\parallel$.

## TIRF emission characteristics

We evaluated fluorescence polarization TIRF microscopy characteristics for excitation, dipole emission near an interface, and light collected into a microscope objective to facilitate

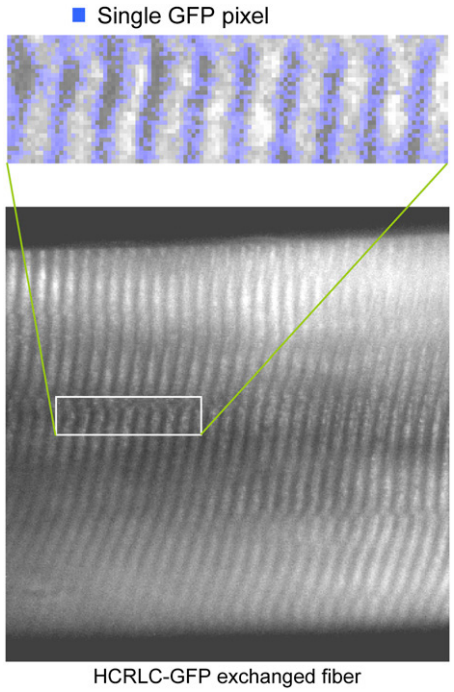


FIGURE 11 (*Top*) Single HCRLC-GFP molecule spatial distribution in the exchanged fiber. Pixels containing single GFP are depicted in blue over the grayscale total fluorescence intensity from the fiber. Single molecules are at the A-band periphery where myosin concentration drops to zero from its peak value of ~300 $\mu$M in the A-band center (*white*). Pixels containing two and more GFPs are distributed closer to the A-band center. (*Bottom*) GFP fluorescence from the entire fiber sample showing where the single HCRLC-GFP image originated.

quantitative interpretation of measurements (42,52). Field intensities in Fig. 6 specify what is needed from excitation to calculate polarized fluorescence intensities from probe orientation. We consider now the effect of the TIR interface on probe emission and collection of light in a high NA microscope objective. The latter mixes light contributions from emitter dipole Cartesian components that become inseparable with an analyzing polarizer unlike with low NA light collection. Axelrod addressed the mixing problem in a homogeneous medium using factors $K_{\|}$, $K_{\perp}$, and $K_{oa}$ ($K$-factors) multiplying squared Cartesian components of the emitter dipole moment parallel or perpendicular to the analyzing polarizer, and parallel to the optical axis of the microscope (43). We address both effects (probe emission perturbation by the TIR interface and light collection by a high NA objective) by reformulated $K$-factors that reduce to Axelrod's results in the limit where there is no discontinuity in the medium separating sample and objective.

Hellen and Axelrod (HA) expanded the dipolar emission field into plane waves reflected and refracted at the interface to describe probe emission perturbation by TIR (42). We added the effect of the high NA objective on collected emitted light polarization. Like HA, we adopted laboratory coordinates with $z$ axis parallel to the optical axis of the inverted microscope pointing into the aqueous medium and with $x$ and $y$ axes in the plane of the interface. HA pointed out that for a fluorophore under steady illumination the dissipated power must equal the absorbed power implying that a fixed-power, rather than a fixed-amplitude, dipole radiator is the appropriate model for probe emission near an interface. The following description employs power normalization.

The emitting probe dipole is located at the focus of the infinity-corrected microscope objective. Decompose the dipole emitted field into the $(p,s,z)$ coordinate system defined as follows. An observation point together with the $z$ axis defines a plane of observation. The value $v_{p,s}$ is the component lying parallel to the interface of any vector $v$ and parallel, perpendicular to the plane of observation. The value $v_z$ is the component perpendicular to the interface. The orientation of the $(p,s,z)$ coordinates depend on azimuthal angle $\varphi$ of the observation point that also defines the objective meridional plane containing unit vectors $p$ and $z$.

Equations 32 and 33 in HA give the $(p,s,z)$ decomposed emitted field as

$$\vec{E} = E_p\hat{p} + E_s\hat{s} + E_z\hat{z}, \tag{3}$$

where

$$\hat{p} = \{Cos[\phi], Sin[\phi], 0\} \tag{4a}$$

$$\hat{s} = \{-Sin[\phi], Cos[\phi], 0\} \tag{4b}$$

$$\hat{z} = \{0, 0, 1\} \tag{4c}$$

$$E_p = (\mu_x Cos[\phi] + \mu_y Sin[\phi])E_p^{\mu_p} + \mu_z E_p^{\mu_z} \tag{4d}$$

$$E_s = (\mu_y Cos[\phi] - \mu_x Sin[\phi])E_s^{\mu_s} \tag{4e}$$

$$E_z = (\mu_x Cos[\phi] + \mu_y Sin[\phi])E_z^{\mu_p} + \mu_z E_z^{\mu_z}, \tag{4f}$$

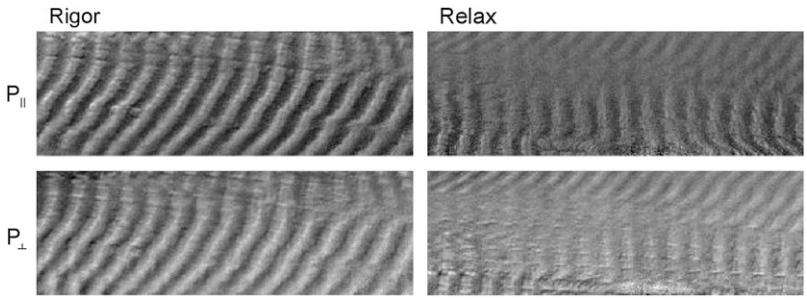


FIGURE 12 Fluorescence polarization ratio images from HCRLC-GFP-tagged muscle fibers in rigor and relaxation. Lighter shades of gray indicate the larger values. Gray scales are identical for a given polarization ratio such that $-0.35 \le P_{\perp} \le 0.25$ and $0 \le P_{\|} \le 0.6$.

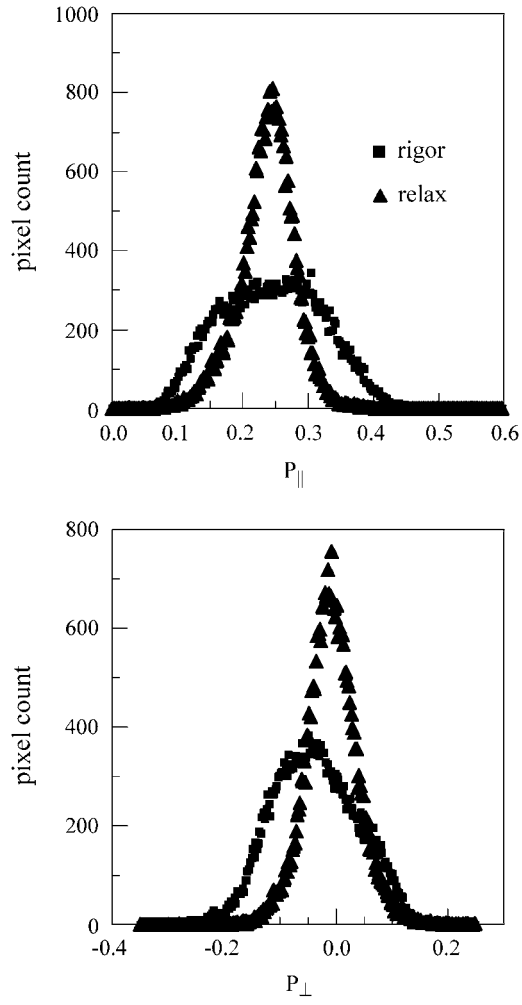


FIGURE 13 Pixel count versus $P_{\|}$ or $P_{\perp}$ histograms for pixels in the images from Fig. 12. Rigor cross-bridges are depicted with solid squares and relaxed cross-bridges with solid triangles in both panels.

and $\mu = (\mu_x,\mu_y,\mu_z)$ is the lab frame Cartesian fluorophore unit-length dipole moment. Field amplitudes $E_i^{\mu_j}$ are the $i^{th}$ component from the dipole component $\mu_j$ and are taken directly from Eq. 26 in HA. The probe electric field formed from Eqs. 3 and 4 has divergent rays propagating toward the objective. They are refracted into plane-polarized light propagating along the optical axis in image space. Application of a particular rotation matrix to the field components (43), or decomposition of the field into components parallel and perpendicular to the meridional plane (53), to preserve field polarization relative to the meridional plane, mimic the effect of a high aperture lens. The two techniques give identical results except that the latter introduces a $\cos^{1/2}\theta$ weighing factor due to the geometrical optics law where $\theta$ is the polar angle an emitted ray makes with the optical axis. The $\cos^{1/2}\theta$ weighting makes a slight change in the *K*-factors reflected in our results.

The objective refracted-plane polarized electric field is projected onto unit vectors parallel to lab *x* or *y* axes to imitate the effect of the analyzing polarizer. These scalars are squared, power-normalized, then integrated over $0 \le \varphi \le 2\pi$ as appropriate for light collection by the objective. *K*-factors are identified as amplitudes multiplying the dipole component products, $\mu_x^2$, $\mu_y^2$, and $\mu_z^2$ in the collected intensity. Cross-terms in dipole components sum to zero with integration over $\varphi$.

Power normalization introduces the amplitude, $(1 + \gamma\mu_z^2)^{-1}$ for $\gamma$ independent of $\mu$, multiplying each squared Cartesian dipole component. The amplitude causes sensitivity in the fluorescence polarization signal to elements of the dipole moment orientation distribution undetected by conventional, i.e., far-field, fluorescence polarization. Power normalization effects have already been discussed in the context of model-independent dipole orientation distribution analysis of fluorescence polarization data (54). We used the model-dependent normal GFP orientation distribution (Eq. 2) where power normalization is treated exactly with $\mu$-dependent *K*-factors. *K*-factors also depend on the distance between emitting dipole and interface. We used *K*-factors averaged over *z* and weighted by the excitation field exponential *z*-axis profile with 100-nm characteristic depth.

Fig. 14 *A* compares *K*-factors derived previously in vacuum and no interface (A/A for Air/Air interface) with those derived as described above for the water/glass (W/G) interface appropriate for the muscle fiber application. Factors are derived for aperture angle $\sigma = \arcsin[NA/1.5]$ on the domain $0 \le NA \le 1.45$. *K*-factors are significant only in their relative value hence we normalize $K_{\|}$ to be identical in the two conditions. The *K*-factors for the A/A and W/G interfaces are similar for low aperture objectives but diverge when NA$\gtrsim$1.2. For NA = 1.45 used in our application to muscle fibers, $K_{oa}$ and $K_{\perp}$, differ substantially between the A/A and W/G cases.

The W/G interface *K*-factors depend on emitting dipole orientation relative to the interface due to emission-dipole-power normalization. Fig. 14 *B* shows the W/G correction factors for $\sigma = \arcsin[1.45/1.5]$ and dipole moments ranging from parallel ($\mu_z = 0$) to perpendicular ($\mu_z = 1$) to the interface.

## DISCUSSION

Myosin lever-arm orientation in muscle has been consistently linked to myosin-based motility. Atomic structures of the MHC N-terminus showed that the lever arm assumed different orientation in the absence (6) and presence (2) of nucleotide and suggested that small conformational changes in the active site induced by ATP hydrolysis are translated by lever arm rotation to the large linear displacements seen in the in vitro motility (55). The idea is consistent with early experiments showing rotary motion within S1 (56–58) and with experiments showing correlation between lever-arm length and the velocity of in vitro motion (59). The MLCs are intimately connected to the lever arm functionality. They

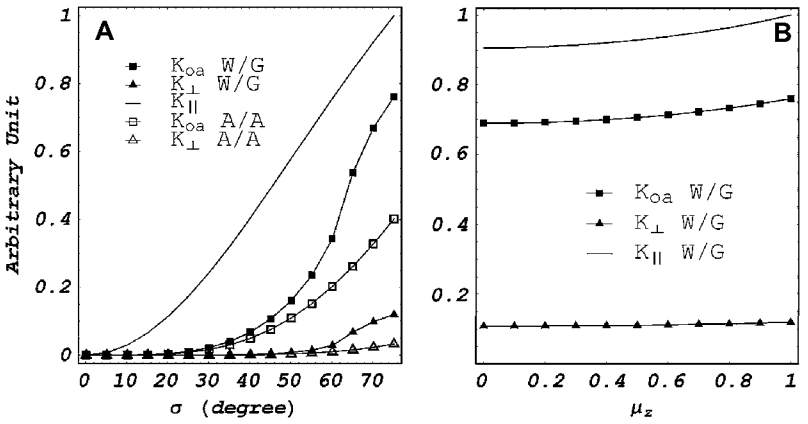


FIGURE 14 (*A*) *K*-factors for no interface separating sample and objective (A/A) and for the water/glass (W/G) interface. Parallel (∥) and perpendicular (⊥) symbols refer to dipole moment components relative to the analyzing polarizer orientation. Subscript *oa* is for the dipole component parallel to the optical axis of the microscope that is perpendicular to any orientation of the analyzing polarizer. Aperture angle $\sigma = \arcsin[\mathrm{NA}/1.5]$ on the domain $0 \le \mathrm{NA} \le 1.45$. *K*-factors are significant only in their relative value, hence we normalize $K_{\|}$ to be identical in the two conditions. *K*-factors for the two cases are similar for low aperture objectives, but diverge when NA$\gtrsim$1.2. (*B*) Effect of dipole orientation on water/glass *K*-factors when $\sigma = \arcsin[1.45/1.5]$. The W/G correction factors for dipole moments ranging from parallel ($\mu_z = 0$) to perpendicular ($\mu_z = 1$) to the interface. The effect follows directly from dipole power normalization.

stabilize the lever arm for efficient work production and are implicated in muscle diseases through regulatory and actin-binding functions. S1 crystal structures showed that lever arm rotation carries bound MLCs through the identical rotational trajectory while their conformations are approximately unchanged. Thus MLC location gives it special sensitivity to lever arm rotation that is often exploited by use of optical spectroscopic probes.

Optical spectroscopic probes are molecular direction sensors due to their selective absorption of exciting light polarized parallel to the probe transition dipole moment. While the selective absorption can be directly detected, most often fluorescence emission from the same transition dipole is collected in a microscope and analyzed for polarization. Emerging in vitro techniques detect protein movement from single fluorophores (32,33), providing more insight into dynamics than the equivalent ensemble-based signal (34,35). In situ, additional forces are in play when the molecules of interest are crowded. A crowded environment produces preferential hydration of a protein thereby favoring lower surface area structures and promoting self-association. We wished to investigate how crowding affects myosin behavior in skeletal muscle fibers. In situ, single molecule isolation requires special attention to defining the smallest possible detection volume. We utilized TIRF microscopy because it provides a means to isolate just a few myosin cross-bridges in the fiber (39).

In TIRF microscopy, excitation laser light is incident on the glass side of a water/glass interface at angles greater than critical angle for TIR. Although light is totally reflected, an evanescent field, created in the water medium and decaying exponentially with distance from the interface, excites fluorophores within ~100 nm of the surface (38). Hellen and Axelrod pointed out that the TIR interface affects probe emission (42). High NA collection of light, typical in single molecule experiments, is known to impair the ability to resolve emitter dipole components using an analyzing polarizer (53). Axelrod showed how to correct for the latter effect using *K*-factors weighting contributions from the emitter dipole Cartesian components, but did not consider the interface-separating sample and objective (present when an oil immersion objective is used) (43). We considered the effect of the TIR interface on probe emission and on collection of light in a high NA microscope objective in one stroke by reformulating the *K*-factors (Fig. 14). Our new *K*-factors reduce to those introduced by Axelrod in the appropriate limit.

Myosin cross-bridges in a muscle fiber are nonuniformly distributed. At the A-band edge, myosin concentration rapidly decreases to zero from a peak value of ~300 $\mu$M (8). We utilized this natural concentration gradient to characterize molecular crowding effects on rigor cross-bridge orientation. Single, double, and multiple GFPs per pixel were identified in the fluorescent muscle fiber image by their signature zero slope in detected photons per pixel versus accumulated photon count threshold (Fig. 8). Single GFPs attached to MLC identified low myosin concentration regions at the A-band edge (Fig. 11). The single GFPs were orientationally ordered such that their dipole moments maintain two distinct polar angles relative to the fiber symmetry axis. The lower angle, where the dipole is nearly parallel to fiber axis, is more highly populated than the alternative larger angle. Both possibilities have a similar distribution width (Fig. 10).

Higher GFP concentrations ($\ge$2 GFPs per detection volume), representative of higher cross-bridge concentration, are oriented in a homogeneous band at ~45° to the fiber axis. The distribution width also narrows in this case, reinforcing the homogeneous characterization of lever arm orientation (Fig. 10). The three observed cross-bridge orientations, two at low concentration and one at high concentration, are distinct. GFP concentration is always very low, even in the middle of the A-band, minimizing the chance that direct GFP/GFP interaction causes the concentration effect. Thus, we find myosin-concentration change correlates with a change in the lever-arm orientation distribution. The effect might be attributed to molecular crowding, since head concentration drops suddenly at the end of the filament or to inhomogeneity in thick filament structure.

The presence of GFP on the lever arm might directly impact lever arm orientation. The impact is minimal at low myosin concentration where mutual myosin/myosin and myosin/GFP

interactions between different cross-bridges (i.e., we are not talking about the GFP interaction with the myosin carrying the HCRLC-GFP) are unlikely. At high myosin concentration, the myosin/GFP interactions might be substantial. We would expect a broadened or multipeaked lever arm orientation distribution due to GFP perturbation of the natural lever-arm orientation. Our experimental results contradict this scenario. Instead of broadening, the lever-arm distribution became more homogeneous at higher myosin concentrations, suggesting the lack of disturbing involvement of our GFP tag. More experience with GPF-tagged HCRLC variants in fibers will be needed to clarify how perturbative GFP is to the natural lever-arm orientation in a muscle fiber.

The idea that molecular crowding influences lever-arm orientation was anticipated based on previous results. Andreev et al. (60) reported that the polarized fluorescence from myosin S1 in rigor complexes in myofibrils differed depending on the relative S1/actin concentration. The fluorescence polarization results were confirmed by cross-linking experiments (61). We showed previously that crowded conditions inhibited S1's physiological MgATPase probably because of an inability to move its lever arm (62). The ability of S1 to present two conformations in solution has been observed in response to temperature change (63,64) and when the active site was trapped by beryllium fluoride and adenosine diphosphate in response to variation of ionic strength (65). In permeabilized muscle fibers, we observed two distinct rigor cross-bridge orientations, again in response to temperature change (66). Open and closed forms observed in S1 crystal structures in the absence and presence of nucleotide, respectively (2,6), might resemble the conformations we observe in rigor fibers. The typical rigor conformation observed in muscle fibers from ensemble-averaged signals (at room temperature) reports what we call here the high-myosin-concentration lever-arm form. It probably corresponds to the open conformation in crystal structures and may also resemble the minor form in the low-myosin-concentration lever-arm orientation. The predominant low-myosin-concentration rigor lever-arm orientation might be the bent lever-arm conformation resembling the closed conformation in crystal structures or akin to another form induced specifically by interaction with F-actin.

Myosin is thought to be a stochastic motor working to move cellular components along actin filaments against a force. In vitro studies have confirmed this supposition by showing single isolated myosin molecules function effectively. Myosin conformation, ATPase, and the molecule's ability to transduce energy are thought to be intimately linked even to the extent that myosin conformation is 1:1, with work producing steps in the cycle (67). If so, our single molecule studies show that this cycle is altered by the crowded environment in the muscle fiber because myosin conformation changes with its concentration. How the cross-bridge might take advantage of this effect is speculative, but the notion that a cross-bridge operates truly stochastically in situ is unlikely.

The GFP-tagged RLC is a probe of the myosin lever arm with potential for detecting lever-arm dynamics in the active cross-bridge of a muscle fiber. We GFP-tagged the human cardiac RLC isoform and exchanged it into a rabbit skeletal muscle fiber. The HCRLC-GFP behaves like the native isoform in this system. Familial hypertropic cardiomyopathy (FHC) is an autosomal dominant disease characterized by a hypertrophic left ventricle in the absence of other causes of cardiac hypertrophy (68). FHC affects 1 in 500 persons and can cause sudden cardiac death in the young (69). Missense mutations in various genes mainly encoding for sarcomeric proteins have been shown to cause the disease (70). These genes include ventricular RLC (MYL2) and ventricular ELC (MYL3). FHC-implicated mutations in RLC or ELC, also exchangeable into rabbit skeletal muscle fibers (71), might affect myosin functionality in fibers. Our GFP-tagged RLC is a probe to assess lever-arm swing characteristics in situ and on the single molecule level.

## CONCLUSION

Single molecule fluorescence polarization was observed from GFP-tagged HCRLC exchanged with the native RLC in permeabilized rabbit skeletal muscle fibers. Single MLC detection within the highly condensed muscle fiber system was accomplished with TIRF microscopy. Evanescent field excitation, SAF detection, and CCD detector pixel size limits detection volume to just a few attoliters. This detection volume occasionally isolates single molecules from the muscle fiber in the microscope field of view under certain HCRLC-GFP exchange conditions. Data analysis manages both the perturbing effect of the TIR interface on probe emission, including dipole emission power normalization, and the effect of high NA collection of light, known to impair the ability to resolve emitter dipole components using an analyzing polarizer. The natural myosin concentration gradient in a muscle fiber allows observation of fluorescence polarization from HCRLC-GFP exchanged myosin at both low and high myosin concentration. In the rigor muscle fiber, cross-bridges at low concentration maintain GFP dipole moments at two distinct polar angles relative to the fiber symmetry axis. The lower angle, where the dipole is nearly parallel to fiber axis, is more highly populated than the alternative larger angle. Cross-bridges at higher concentration are oriented in a homogeneous band at $\sim 45^\circ$ to the fiber axis. All three orientations, two at low concentration and one at high concentration, are distinct. The data demonstrates that myosin concentration has an impact on myosin conformation, suggesting mutual interactions between cross-bridges are altering how the muscle generates force. The GFP-tagged RLC is a novel probe to assess single lever-arm orientation characteristics in situ and may be useful in future applications assessing how FHC-implicated mutations of the MLCs affect muscle functionality.

## SUPPLEMENTARY MATERIAL

To view all of the supplemental files associated with this article, visit www.biophysj.org.

We gratefully acknowledge Dr. D. Szczesna-Cordary, University of Miami, for the generous gift of the HCRLC cDNA.

This work was supported by National Institutes of Health-National Institute of Arthritis and Musculoskeletal and Skin Diseases grant No. R01AR049277 and the Mayo Foundation.

## REFERENCES

1. Houdusse, A., and C. Cohen. 1996. Structure of the regulatory domain of scallop myosin at 2 Å resolution: implications for regulation. *Structure*. 4:21–32.
2. Dominguez, R., Y. Freyzon, K. M. Trybus, and C. Cohen. 1998. Crystal structure of a vertebrate smooth muscle myosin motor domain and its complex with the essential light chain: visualization of the pre-power stroke state. *Cell*. 94:559–571.
3. Highsmith, S. 1999. Lever arm model of force generation by actin-myosin-ATP. *Biochemistry*. 38:9792–9797.
4. Huxley, H. E. 1969. The mechanism of muscular contraction. *Science*. 164:1356–1366.
5. Eisenberg, E., and T. L. Hill. 1985. Muscle contraction and free energy transduction in biological systems. *Science*. 227:999–1006.
6. Rayment, I., W. R. Rypniewski, K. Schmidt-Base, R. Smith, D. R. Tomchick, M. M. Benning, D. A. Winkelmann, G. Wesenberg, and H. M. Holden. 1993. Three-dimensional structure of myosin subfragment-1: a molecular motor. *Science*. 261:50–58.
7. Nelson, D. L., and M. M. Cox. 2005. Protein Function. *In* Lehninger: Principles of Biochemistry. W.H. Freeman and Company, New York.
8. Tikunov, B. A., H. L. Sweeney, and L. C. Rome. 2001. Quantitative electrophoretic analysis of myosin heavy chains in single muscle fibers. *J. Appl. Physiol.* 90:1927–1935.
9. Wagner, P. D., and A. G. Weeds. 1977. Studies on the role of myosin alkali light chains. Recombination and hybridization of light chains and heavy chains in subfragment 1 preparations. *J. Mol. Biol.* 109:455–470.
10. Wagner, P. D. 1981. Formation and characterization of myosin hybrids containing essential light chains and heavy chains from different muscle myosins. *J. Biol. Chem.* 256:2493–2498.
11. Arata, T. 1990. Orientation of spin-labeled light chain 2 of myosin heads in muscle fibers. *J. Mol. Biol.* 214:471–478.
12. Irving, M., T. S. C. Allen, C. Sabido-David, J. S. Cralk, B. Brandmeler, J. Kendrick-Jones, J. E. T. Corrie, D. R. Trentham, and Y. E. Goldman. 1995. Tilting of the light-chain region of myosin during step length changes and active force generation in skeletal muscle. *Nature*. 375:688–690.
13. Brack, A. S., B. Brandmeier, R. E. Ferguson, S. Criddle, R. Dale, and M. Irving. 2004. Bifunctional rhodamine probes of myosin regulatory light chain orientation in relaxed skeletal muscle fibers. *Biophys. J.* 86:2329–2341.
14. Borejdo, J., D. S. Ushakov, and I. Akopova. 2002. Regulatory and essential light chains of myosin rotate equally during contraction of skeletal muscle. *Biophys. J.* 82:3150–3159.
15. Yang, F., L. J. Moss, and G. N. Phillips, Jr. 1996. The molecular structure of green fluorescent protein. *Nat. Biotechnol.* 14:1246–1251.
16. Ormo, M., A. B. Cubitt, K. Kallio, L. A. Gross, R. Y. Tsien, and S. J. Remington. 1996. Crystal structure of the *Aequorea victoria* green fluorescent protein. *Science*. 273:1392–1395.
17. Cubitt, A. B., R. Heim, S. R. Adams, A. E. Boyd, L. A. Gross, and R. Y. Tsien. 1995. Understanding, improving and using green fluorescent proteins. *Trends Biochem. Sci.* 20:448–455.
18. Chalfie, M., Y. Tu, G. Euskirchen, W. W. Ward, and D. C. Prasher. 1994. Green fluorescent protein as a marker for gene expression. *Science*. 263:802–805.
19. Rosell, F. I., and S. G. Boxer. 2003. Polarized absorption spectra of green fluorescent protein single crystals: transition dipoles moment directions. *Biochemistry*. 42:177–183.
20. Inoué, S., O. Shimomura, M. Goda, M. Shribak, and P. T. Tran. 2002. Fluorescence polarization of green fluorescence protein. *Proc. Natl. Acad. Sci. USA*. 99:4272–4277.
21. Rocheleau, J. V., M. Edidin, and D. W. Piston. 2003. Intrasequence GFP in class I MHC molecules, a rigid probe for fluorescence anisotropy measurements of the membrane environment. *Biophys. J.* 84: 4078–4086.
22. Burghardt, T. P., T. Ando, and J. Borejdo. 1983. Evidence for cross-bridge order in contraction of glycerinated skeletal muscle. *Proc. Natl. Acad. Sci. USA*. 80:7515–7519.
23. Huxley, A. F., and R. M. Simmons. 1971. Proposed mechanism of force generation in striated muscle. *Nature*. 233:533–538.
24. Tanner, J. W., D. D. Thomas, and Y. E. Goldman. 1992. Transients in orientation of a fluorescent cross-bridge probe following photolysis of caged nucleotides in skeletal muscle fibers. *J. Mol. Biol.* 223:185–203.
25. Burghardt, T. P., S. P. Garamszegi, and K. Ajtai. 1997. Probes bound to myosin Cys-707 rotate during length transients in contraction. *Proc. Natl. Acad. Sci. USA*. 94:9631–9636.
26. Hopkin, S. C., C. Sabido-David, U. A. van der Heide, R. E. Ferguson, B. D. Brandmeier, R. E. Dale, J. Kendrick-Jones, J. E. T. Corrie, D. R. Trentham, M. Irving, and Y. E. Goldman. 2002. Orientation changes of the myosin light chain domain during filament sliding in active and rigor muscle. *J. Mol. Biol.* 318:1275–1291.
27. St. Claire Allen, T., N. Ling, M. Irving, and Y. E. Goldman. 1996. Orientation changes in myosin regulatory light chains following photorelease of ATP in skinned muscle fibers. *Biophys. J.* 70:1847–1862.
28. Shepard, A., and J. Borejdo. 2004. Correlation between mechanical and enzymatic events in contracting skeletal muscle fiber. *Biochemistry*. 43:2804–2811.
29. Feher, G., and M. Weissman. 1973. Fluctuations spectroscopy: determination of chemical reaction kinetics from the frequency spectrum of fluctuations. *Proc. Natl. Acad. Sci. USA*. 70:870–875.
30. Elson, E. L. 1974. Fluorescence correlation spectroscopy. I. Conceptual basis and theory. *Biopolymers*. 13:1–27.
31. Starr, T. E., and N. L. Thompson. 2002. Local diffusion and concentration of IgG near planar membranes: measurement by total internal reflection with fluorescence correlation spectroscopy. *J. Phys. Chem. B*. 106:2365–2371.
32. Yildiz, A., and P. R. Selvin. 2005. Fluorescence imaging with one nanometer accuracy: application to molecular motors. *Acc. Chem. Res.* 38:574–582.
33. Rosenberg, S. A., M. E. Quinlan, J. N. Forkey, and Y. E. Goldman. 2005. Rotational motions of macromolecules by single-molecule fluorescence microscopy. *Acc. Chem. Res.* 38:583–593.
34. Neuweiler, H., and M. Sauer. 2005. Exploring life by single-molecule fluorescence spectroscopy. *Anal. Chem.* 77:179A–185A.
35. Dunn, R. C. 1999. Near-field scanning optical microscopy. *Chem. Rev.* 99:2891–2927.
36. Minton, A. P. 2001. The influence of macromolecular crowding and macromolecular confinement on biochemical reactions in physiological media. *J. Biol. Chem.* 276:10577–10580.
37. Timasheff, S. N. 2002. Protein-solvent preferential interactions, protein hydration, and the modulation of biochemical reactions by solvent components. *Proc. Natl. Acad. Sci. USA*. 99:9721–9726.
38. Axelrod, D. 2001. Total internal reflection fluorescence microscopy in cell biology. *Traffic*. 2:764–774.
39. Burghardt, T. P., K. Ajtai, and J. Borejdo. 2006. In situ single molecule imaging with attoliter detection using objective total internal reflection confocal microscopy. *Biochemistry*. 45:4058–4068.
40. Ruckstuhl, T., and S. Seeger. 2003. Confocal total-internal-reflection fluorescence microscopy with a high-aperture parabolic mirror lens. *Appl. Opt.* 42:3277–3283.

41. Borejdo, J., J. Talent, I. Akopova, and T. P. Burghardt. 2006. Rotations of a few cross-bridges in muscle by confocal total internal reflection microscopy. *Biochim. Biophys. Acta.* 1763:137–140.

42. Hellen, E. H., and D. Axelrod. 1987. Fluorescence emission at dielectric and metal-film interfaces. *J. Opt. Soc. Am. B.* 4:337–350.

43. Axelrod, D. 1979. Carbocyanine dye orientation in red cell membrane studied by microscopic fluorescence polarization. *Biophys. J.* 26:557–573.

44. Szczesna, D., D. Ghosh, Q. Li, A. V. Gomes, G. Guzman, C. Arana, G. Zhi, J. T. Stull, and J. D. Potter. 2001. Familial hypertrophic cardiomyopathy mutations in the regulatory light chains of myosin affect their structure, $Ca^{2+}$ binding, and phosphorylation. *J. Biol. Chem.* 276: 7086–7092.

45. Borejdo, J., S. Putnam, and M. F. Morales. 1979. Fluctuations in polarized fluorescence: Evidence that muscle cross bridges rotate repetitively during contraction. *Proc. Natl. Acad. Sci. USA.* 76:6346–6350.

46. Sabido-David, C., B. Brandmeier, J. S. Craik, J. E. T. Corrie, D. R. Trentham, and M. Irving. 1998. Steady-state fluorescence polarization studies of the orientation of myosin regulatory light chains in single skeletal muscle fibers using pure isomers of iodoacetamidotetramethylrhodamine. *Biophys. J.* 74:3083–3092.

47. Ajtai, K., P. J. K. Ilich, A. Ringler, S. S. Sedarous, D. J. Toft, and T. P. Burghardt. 1992. Stereospecific reaction of muscle fiber proteins with the 5′ or 6′ isomer of iodoacetamidotetramethyl rhodamine. *Biochemistry.* 31:12431–12440.

48. Burghardt, T. P., and N. L. Thompson. 1984. Evanescent intensity of a focused Gaussian light beam undergoing total internal reflection in a prism. *Opt. Eng.* 23:62–67.

49. Kneen, M., J. Farinas, Y. Li, and A. S. Verkman. 1998. Green fluorescent protein as a noninvasive intracellular pH indicator. *Biophys. J.* 74:1591–1599.

50. Cantor, C. R., and P. R. Schimmel. 1980. Techniques for the study of biological structure and function. W. H. Freeman, New York.

51. Damser, G., and C. M. Waterman-Storer. 2006. Quantitative fluorescent speckle microscopy of cytoskeleton dynamics. *Annu. Rev. Biophys. Biomol. Struct.* 35:361–387.

52. Axelrod, D., E. H. Hellen, and R. M. Fulbright. 1992. Total internal reflection fluorescence. *In* Topics in Fluorescence Spectroscopy, Vol. 3, Biomedical Applications. J. R. Lakowicz, editor. Plenum, New York.

53. Richards, B., and E. Wolf. 1959. Electromagnetic diffraction in optical systems. II. Structure of the image field in an aplanatic system. *Proc. Roy. Soc. A.* 253:358–379.

54. Thompson, N. L., and T. P. Burghardt. 1986. Total-internal reflection fluorescence: measurement of spatial and orientational distributions of fluorophores near planar dielectric interfaces. *Biophys. Chem.* 25:91–97.

55. Geeves, M. A., and K. C. Holmes. 1999. Structural mechanism of muscle contraction. *Annu. Rev. Biochem.* 68:687–728.

56. Highsmith, S., and D. Eden. 1993. Myosin-ATP chemomechanics. *Biochemistry.* 32:2455–2458.

57. Wakabayashi, K., M. Tokunaga, I. Kohno, Y. Sugimoto, T. Hamanaka, Y. Takezawa, T. Wakabayashi, and Y. Amemiya. 1992. Small-angle synchrotron x-ray scattering reveals distinct shape changes of the myosin head during hydrolysis of ATP. *Science.* 258:443–447.

58. Aguirre, R., S. H. Lin, F. Gonsoulin, C. K. Wang, and H. C. Cheung. 1989. Characterization of the ethenoadenosine diphosphate binding site of myosin subfragment 1. Energetics of the equilibrium between two states of nucleotide-S1 and vanadate-induced global conformation changes detected by energy transfer. *Biochemistry.* 28:799–807.

59. Uyeda, T. Q. P., P. D. Abramson, and J. A. Spudich. 1996. The neck region of the myosin motor domain acts as a lever arm to generate movement. *Proc. Natl. Acad. Sci. USA.* 93:4459–4464.

60. Andreev, O. A., R. Takashi, and J. Borejdo. 1995. Fluorescence polarization study of the rigor complexes formed at different degrees of saturation of actin filaments with myosin subfragment-1. *J. Muscle Res. Cell Motil.* 16:353–367.

61. Andreev, O. A., and J. Borejdo. 1995. Binding of heavy-chain and essential light-chain 1 of S1 to actin depends on the degree of saturation of F-actin filaments with S1. *Biochemistry.* 34:14829–14833.

62. Peyser, Y. M., S. Shaya, K. Ajtai, T. P. Burghardt, and A. Muhlrad. 2003. Cosolvent induced aggregation inhibits myosin ATPase activity by stabilizing the predominant transition intermediate. *Biochemistry.* 42:12669–12675.

63. Shriver, J. W., and B. D. Sykes. 1981. Phosphorus-31 nuclear magnetic resonance evidence for two conformations of myosin subfragment-1-nucleotide complexes. *Biochemistry.* 20:2004–2012.

64. Shriver, J. W., and B. D. Sykes. 1981. Energetics and kinetics of interconversion of two myosin subfragment-1-adenosine 5′-diphosphate complexes as viewed by phosphorus-31 nuclear magnetic resonance. *Biochemistry.* 20:6357–6362.

65. Peyser, Y. M., K. Ajtai, T. P. Burghardt, and A. Muhlrad. 2001. Effect of ionic strength on the conformation of myosin subfragment 1-nucleotide complexes. *Biophys. J.* 81:1101–1114.

66. Ajtai, K., and T. P. Burghardt. 1986. Observation of two orientations from rigor cross-bridges in glycerinated muscle fibers. *Biochemistry.* 25:6203–6207.

67. Geeves, M. A., R. Fedorov, and D. J. Manstein. 2005. Molecular mechanism of actomyosin-based motility. *Cell. Mol. Life Sci.* 62: 1462–1477.

68. Richardson, P., W. McKenna, M. Bristow, B. Maisch, B. Mautner, J. O'Connell, E. Olsen, G. Thiene, J. Goodwin, I. Gyarfas, I. Martin, and P. Nordet. 1996. Report of the 1995 WHO/ISFK task force on the definition and classification of cardiomyopathies. *Circulation.* 93: 841–842.

69. Maron, B. J., J. M. Gardin, J. M. Flack, S. S. Gidding, T. T. Kurosaki, and D. E. Bild. 1995. Prevalence of hypertrophic cardiomyopathy in a general population of young adults: echocardiographic analysis of 4111 subjects in the CARDIA study. *Circulation.* 92:785–789.

70. Seidman, J. G., and C. Seidman. 2001. The genetic basis for cardiomyopathy: from mutation identification to mechanistic paradigms. *Cell.* 104:557–567.

71. Sweeney, H. L. 1995. Function of the N-terminus of the myosin essential light chain of vertebrate striated muscle. *Biophys. J.* 68: 112s–119s.